Plasmonic Point-of-Care Device for Sepsis Biomarker Detection

Souvik Kundu, Shawana Tabassum, and Ratnesh Kumar, *Fellow, IEEE*

***Abstract*—The need for point-of-care (POC) devices for detecting the onset of sepsis has become critical since sepsis is one of the most prevalent causes of deaths worldwide in non-coronary intensive care units at the hospitals. Every one hour delay in exercising proper medication can lead to an exponential rise in mortality. Motivated by this, we propose a POC device for sepsis biomarker detection, which will complement traditional blood culture-based techniques for easy and quicker diagnosis and monitoring of sepsis state. The working principle of the device is based on amalgamation of surface plasmon resonance (SPR) technology with microfluidics. The sensing chip consists of a gold and graphene oxide coated patterned array of periodic nanoposts to detect target biomarker molecules in a limited sample volume. The nanoposts are functionalized with specific receptor molecules that serve as a nanostructured plasmonic crystal for SPR-based bio-sensing via the excitation of surface plasmon polaritons. The sensitivity of the device to one of the known sepsis biomarkers, Pro-calcitonin (PCT), was found to be 0.0643 a.u./ pg.ml^{-1} at lower concentration and 0.0224 a.u./ pg.ml^{-1} at higher concentration, and a LOD of 1.22 pg.ml^{-1}. The sensor chip provides an opportunity to dynamically measure antigen-antibody bindings and the soft-lithography based sensor manufacturing technology provides high reproducibility of the sensor response to PCT molecules even at a picomolar level. The microfluidics-based platform provides potential for future integration with other microfluidic devices viz. plasma separator for separating the PCT-sized molecules to enable blood sample measurements**

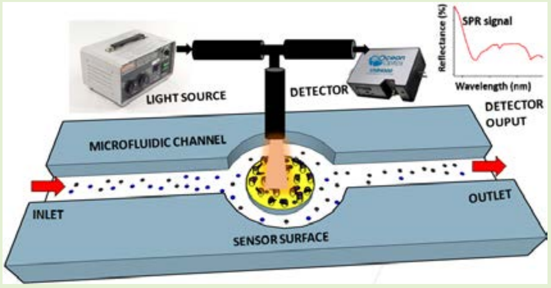

***Index Terms*—Bio-markers, biosensor, plasmonics, point-of-care (PoC), sepsis, surface plasmon resonance.**

I. INTRODUCTION

THERE are more than 31.5 million people who suffer from sepsis every year around the world. Among them, 19.4 million develop severe sepsis and about 5.3 million people die [1]. Further, it has been estimated that there are about 3 million sepsis cases in newborn babies and 1.2 million in children per year globally, with mortality rates between 11% and 19% [2]. As stated by [3], the cause of these grim numbers is due to the lack of an prompt, accurate and point-of-care (POC) sepsis diagnosis method.

A concise discussion on the sepsis pathogenesis, impact, diagnosis and a review of state of the art diagnostic techniques and its limitations can be found in [4]. Traditional sepsis testing involves blood, bronchial fluid, cerebrospinal fluid (CSF) and urine culture. Due to typical prolonged blood culture turnaround time of around 24-72 hrs (from specimen collection to actionable test results), septic patients may progress toward septic shock along with multi organ dysfunction (MoD) [5]. Each hour of delay in exercising an appropriate anti-microbial medicine to the patients results in 7.6% decline in the survival rate of a patient [6]. Also, statistically the diagnostic accuracy of the traditional blood culture based methodologies improve with higher volume of extracted patient blood [7]. However, for critical care patients, extraction of sufficient amount of blood for testing is often not possible which is another challenge for conventional blood-culture based diagnosis of sepsis. Measurements of leukocytes or C-reactive proteins (CRP) are also conducted to identify an infection. However, elevated leukocytes or CRP may also correspond to clinical conditions other than sepsis [8]. Thus, there is an urgent need for rapid and bedside monitoring of sepsis with limited blood volume.

Several label-free detection techniques have been employed for sepsis biomarker detection ranging from electrochemical [9], optical [10], field effect transistor-based [11], acoustic [12], and microfluidic-based [13]. Although electrochemical sensors provides higher sensitivity, but generally

Manuscript received April 17, 2021; revised May 10, 2021; accepted May 15, 2021. Date of publication June 11, 2021; date of current version August 31, 2021. This work was supported by the National Science Foundation under Grant NSF-CCF-1331390, Grant NSF-ECCS-1509420, Grant NSF-PFI-1602089, and Grant NSF-CSSI-2004766. The associate editor coordinating the review of this article and approving it for publication was Dr. Ioannis Raptis. *(Corresponding author: Souvik Kundu.)*

Souvik Kundu and Ratnesh Kumar are with the Department of Electrical and Computer Engineering (ECE), Iowa State University (ISU), Ames, IA 50011 USA (e-mail: souvik@iastate.edu; rkumar@iastate.edu).

Shawana Tabassum is with the Department of Electrical Engineering (EE), The University of Texas at Tyler (UTT), Tyler, TX 75799 USA (e-mail: stabassum@uttyler.edu).

Digital Object Identifier 10.1109/JSEN.2021.3088117

1558-1748 © 2021 IEEE. Personal use is permitted, but republication/redistribution requires IEEE permission.
See https://www.ieee.org/publications/rights/index.html for more information.

these sensors provide little information on binding kinetics of protein-protein interactions on the sensor surface [14]. This limitation can be overcome by our microfluidic plasmonic sensor, as proposed in this work. It allows us to quantify the protein–protein binding affinity by studying binding kinetics represented by the sensorgram, which helps in designing and implementing a better target antibody for a given antigen [15]. Among various biomarkers including CRP and interlukin-6, procalcitonin (PCT) is most commonly used biomarker for identifying bacterial sepsis [16]. The concentration of PCT in normal human being is less than 10pg/ml and the concentration can rise from 10 to 10,000 pg/ml during sepsis condition. Therefore, we have used our microfluidics plasmonic biochip for detecting PCT in a buffer solution in the above concentration range, and have demonstrated the application of our sensor for measuring the sepsis biomarker PCT.

Point-of-Care solution to biomarker detection/diagnosis in blood samples can be broken up into two steps: Extraction of plasma from blood (which removes the larger molecules such as red blood cells, white blood cells and platelets from blood), and detection/diagnosis of the analyte biomarkers in plasma. There already exist several POC approaches to extract plasma from blood [17], [18], and here we provide POC approach for detecting/diagnosis sepsis biomarker in blood plasma and spiked buffer analyte solution (a common practice as for example also in the works of [19]–[21]). It will be possible to integrate the plasma extraction step with our proposed biochip, and the current work focuses on providing a proof-of-concept for POC sepsis biomarker PCT detection. Accordingly, in this paper we have provided:

- Detailed fabrication process for the microfluidic plasmonic biosenosr chip;
- Analysis of mode of surface plasmon resonance of the sensor, and estimation of sensitivity w.r.t. the changes in surrounding refractive indices;
- SPR measurements with PCT protein at different flow rates and demonstration of the real-time monitoring of the kinetics of protein-protein binding at the sensor surface;
- Exposition of the specificity of our sensor to PCT, with negligible rate of change of sensor response to non-specific proteins in human plasma;
- Comparison of performance of the proposed sensor w.r.t. the sensors reported in literature for the PCT detection.

II. PLASMONIC SENSOR WORKING PRINCIPLE

An electromagnetic wave impinging on a metal-dielectric interface gives rise to collective oscillations of free electrons, which leads to the formation of surface waves called surface plasmon polaritons (SPP) [22]. However, electromagnetic radiation by itself cannot attain SPP resonance due to absence of momentum match between the incident radiation and that of surface plasmons (SP). For a resonance to occur, the component of the wave vector of the incident radiation along the interface should equal the wave vector of the SP. Thus in order to attain SPP resonance several configurations have been employed [23] viz. Kretschmann configuration, Otto configuration, waveguide SPR, and grating coupling.

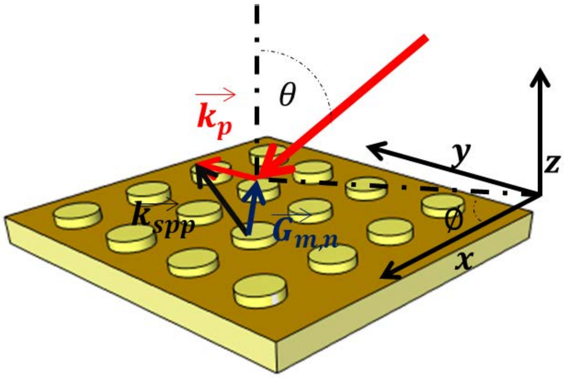

Fig. 1. Nano-post induced SPP excitation: Schematic illustration of the nanopost array on which incident light with in-plane wavevector $\vec{k}_p$ couples to the Grating momentum vector $\vec{G}_{m,n}$ supported by the structure resulting in the $(\vec{m,n})$ Bloch-SPP mode being excited and propagating in the direction of $\vec{k}_{spp}$ [24].

A. Grating Coupled Surface Plasmon Resonance

In our work, we have employed grating coupling configuration for the momentum matching using a 2-D array of nanoposts having diameter, pitch, and depth of 250 nm, 500 nm, and 210 nm respectively.

Fig. 1 depicts the generation of SPP wave vector, $\vec{k}_{spp}$, by the in-plane wave vector of the incident radiation, $\vec{k}_p$, and the Grating momentum wave vector, $\vec{G}_{m,n}$, as in (1):

$$\vec{k}_{spp} = \vec{k}_p + \vec{G}_{m,n}. \tag{1}$$

The grating wave-vector is defined by (2), where Λ denotes the pitch of the square lattice of the nanopost array (lattice constant), and the order of SPP is given by (m, n).

$$\vec{G}_{m,n} = m\frac{2\pi}{\Lambda}\hat{x} + n\frac{2\pi}{\Lambda}\hat{y}. \tag{2}$$

The in-plane wave vector of incident radiation is given by (3), where θ is the angle of incidence and ϕ is the azimuthal angle, illustrated in Fig. 1:

$$\vec{k}_p = m\frac{2\pi}{\lambda}\sin(\theta)\cos(\phi)\hat{x} + n\frac{2\pi}{\lambda}\sin(\theta)\sin(\phi)\hat{y}. \tag{3}$$

$\vec{k}_{spp}$ is the wave vector of the generated surface wave that propagates along the metal-dielectric interface. $\vec{k}_{spp}$ is a function of dielectric permittivity of both metal (ϵ_m) and dielectric (ϵ_d) and is given by

$$\vec{k}_{spp} = \frac{2\pi}{\lambda}\sqrt{\frac{\epsilon_d\epsilon_m}{\epsilon_d + \epsilon_m}}.$$

Combining (1)-(3), at resonant wavelength, $\lambda = \lambda_{spp_{m,n}}$, corresponding to mode (m, n) of SPP, the condition in (4) must be satisfied:

$$\begin{aligned}\frac{2\pi}{\lambda}\sqrt{\frac{\epsilon_d\epsilon_m}{\epsilon_d + \epsilon_m}} &= \Bigg|m\frac{2\pi}{\lambda}\sin(\theta)\cos(\phi)\hat{x} + n\frac{2\pi}{\lambda}\sin(\theta)\sin(\phi)\hat{y} \\ &\quad + m\frac{2\pi}{\Lambda}\hat{x} + n\frac{2\pi}{\Lambda}\hat{y}\Bigg|.\end{aligned} \tag{4}$$

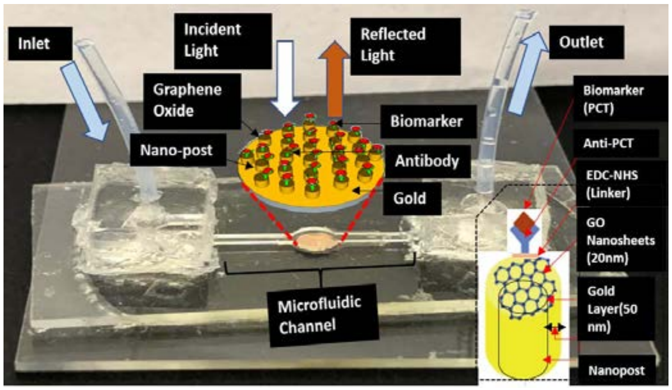

Fig. 2. Fabricated sepsis microfluidic biochip.

(4) can be rewritten by evaluating the magnitude of the right hand side to find the resonant wavelength as given by (5):

$$\frac{2\pi}{\lambda}\sqrt{\frac{\epsilon_d\epsilon_m}{\epsilon_d+\epsilon_m}} = 2\pi\sqrt{\left(\frac{m}{\Lambda}+\frac{\sin(\theta)\cos(\phi)}{\lambda}\right)^2+\left(\frac{n}{\Lambda}+\frac{\sin(\theta)\sin(\phi)}{\lambda}\right)^2}. \tag{5}$$

For our experimental set up, the incident radiation was taken to be normal to the x-y plane, hence by setting $\theta = 0°$ and squaring both sides of (5), we obtain the simplified form (6) for the resonant wavelength corresponding to our sensor structure's SPP excitation mode.

$$\lambda_{spp_{m,n}} = \frac{\Lambda}{\sqrt{m^2+n^2}}\sqrt{\frac{\epsilon_d\epsilon_m}{\epsilon_d+\epsilon_m}}. \tag{6}$$

B. Working Principle of the Proposed Sensor

Any changes in the dielectric permitivity that occurs in the surrounding medium, results in a change in the surface plasmon coupling condition due to a change in permittivity at the metal-dielectric interface. The surface plasmon waves that are excited at the metal-dielectric interface, propagate along the surface, and respond to changes in surrounding electrical permitivity caused by capture of analyte on the surface (in our case Procalcitonin (PCT), a sepsis biomarker). The changes in permittivity can be detected in three different ways: (a) measuring changes in coupling angle at a fixed resonant wavelength, (b) measuring changes in coupling λ at a fixed angle, or (c) measuring change in intensity of transmitted/reflected light at fixed wavelength and angle. In this work, we used (c), i.e., measured shifts in the reflected light intensity at the resonance wavelength of our sensor structure and at normal incidence.

III. SENSOR FABRICATION AND FUNCTIONALIZATION

Fig. 2 depicts the fabricated portable, plasmonic biochip at the POC for quantification of PCT protein. The buffer solution spiked with the PCT protein is injected through the inlet and the solution reaches the sensor surface through a microfluidic channel. The sensor surface is a grating structure of pitch 500 nm containing nanoposts (height 210 nm, diameter 250 nm) coated with gold, graphene oxide (GO), and functionalized with anti-PCT, resulting in SPR resonance in visible range as desired (at 637 nm). The nanoposts are first coated with gold of thickness 50 nm. Next, in order to functionalize the gold nanopost sensor surface with anti-PCT protein, graphene oxide is deposited. For this the gold nanopost array was drop coated with a 20 nm thick layer of GO nanosheets. Graphene oxide consists of covalently attached oxygen-containing functional groups such as hydroxyl, epoxy, carbonyl and carboxyl groups that allow binding with anti-PCT. The periodic GO-Au nanopost array was next functionalized with anti-PCT molecules via EDC-NHS coupling chemistry [25]. A schematic diagram of the nanopost along with all layers is illustrated in the inset of Fig. 2. Light is shone on the grated sensor surface from a white light source and the reflected light is detected by a spectrometer. It is worth mentioning here that the thickness of the gold layer was chosen to maximize the quality factor Q of the resonance. (The resonant wavelength itself is a function of the pitch of the nanoposts and permittivity's of gold vs. nanoposts, but is unaffected by its depth.) The quality factor of resonance is defined as the ratio of the stored energy to the energy dissipated. At an optimal thickness, the energy lost by the collision among the oscillatory plasmons is minimized, thereby maximizing the overall quality factor. This is confirmed in [26] where the sharpness of resonance is studied as the metal (Au) layer thickness is varied. The lowest value of the reflection minima is achieved at around 50 nm gold layer thickness. Accordingly, we have chosen the gold layer of 50nm thickness. The reflected light carries information on the binding kinetics of biomolecular interactions at the surface of the biosensor. A continuous flow rate for a given amount of time is maintained using a syringe pump and the remaining protein solution is collected at the outlet via a vial.

A. Sensor Fabrication

A soft lithography based replica nanomolding technique is employed to fabricate the sensor. In order to form the grating structure, an array of polymeric nanoposts was created followed by graphene oxide deposition and immobilization of anti-PCT molecules, followed by the formation of microfluidic channel, inlet, and outlet ports. Fig. 3(a)-(e) illustrates the detailed fabrication steps.

First, a silicon (Si) master mold was fabricated using electron-beam lithography and reactive ion etching is done after that. Salinization was done for approximately twenty minutes with the help of (tridecafluoro-1,1,2,2-tetrahydrooctyl)-1-trichlorosilane. We employed a two-step process for polydimethylsiloxane (PDMS) mold preparation from the Si master mold. Firstly, we have mixed poly (7– 8% vinylmethyl-siloxane)-(dimethylsiloxane), (1,3,5,7-tetravinyl1,3,5,7-tetramethylcyclotetrasiloxane), platinum catalyst xylene and poly (25–30% methylhydrosiloxane)-(dimethylsiloxane) at a weight ratio of 3.4 : 0.1 : 0.05 : 1 to prepare a hard-PDMS (h-PDMS) precursor solution. Next, mixture was degassed for about ten minutes to remove air bubbles. After that, the hard-PDMS solution was

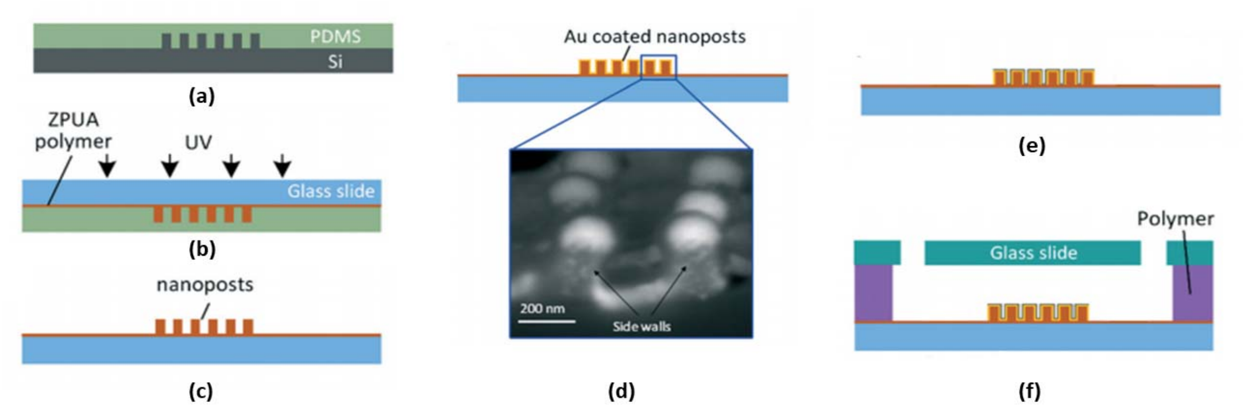

Fig. 3. Fabrication steps: (a)–(f) Step-wise representation for the fabrication of sepsis biosensor. The SEM image for the gold coating on the sidewalls of nanoposts is given by inset of (d).

spun-coated on the Si surface of master mold at 1000 rpm for 40 s. It was then subsequently cured for ten minutes at 70°C. Next, to make a soft-PDMS (s-PDMS) pre-polymer solution, Sylgard 184 monomer and it's curing agent were mixed at the weight ratio of 10 : 1 followed by degassing for about 30 min. Then the s-PDMS solution was poured over cured h-PDMS and the combination was cured for 2 hrs at 65°C as shown in Fig. 3(a). Finally, the cured PDMS mold was peeled off from the Si master mold and thus a complimentary nanohole structure was formed on the PDMS mold. The above two step process of mold preparation is significant because generally the pre-polymer solution of s-PDMS has a higher viscosity which makes it hard for the solution to enter the nanostructures fully at the surface of the Si mold. However, one can argue that if we increase the weight ratio of the monomer to curing agent, it can decrease the viscosity, but in that case the cured PDMS structure would be difficult to peel off from the Si mold without damage. The h-PDMS precursor solution is relatively less viscos than s-PDMS and therefore conforms well along with the nano-structured surface of the Si mold. Hence h-PDMS helps in better conformation and the s-PDMS facilitates easy peeling off the PDMS mold from the Si mold.

In order to transfer the nanostructures from the PDMS mold to a glass substrate, an ultra-violet (UV) curable ZPUA precursor solution procured from Gelest, Inc. was drop cast over the PDMS mold and then the PDMS mold was placed over a glass slide. For curing the ZPUA, the combination of glass and mould was exposed for 5 min to a UV light of intensity 3.3 mW cm^{-2} to form the periodic array of ZPUA nanoposts as shown in Fig. 3(b) and (c). Finally, a 5 nm thick titanium layer was deposited by e-beam evaporation to provide good adhesion to the continuing thickness build up of the 80 nm thick gold layer deposited next on the ZPUA nanoposts array, as illustrated in Fig. 3(d). Next the sample substrates were mounted on a rotating and tilting substrate holder for improving the sidewall gold deposition coverage on the nanoposts. This sidewall coverage of gold on the nanoposts was confirmed from the scanning electron microscopic (SEM) image (Fig. 3(d)).

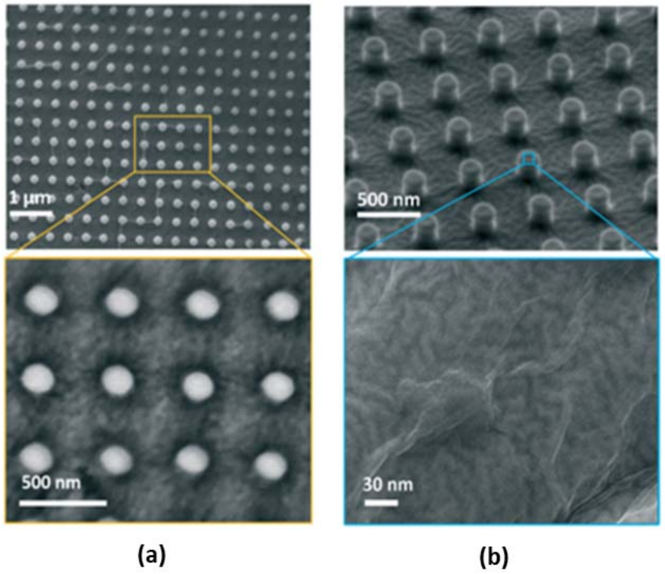

Fig. 4. SEM characterization [29] (a) the Gold(Au) nanoposts array (b) graphene oxide(GO) coated gold(Au) nanopost array.

An *in situ* liquid phase polymerization process [27] was performed for the integration of the SPR sensor inside a microfluidic channel, that is made of a photo-patternable polymer [28]. In this step, to make an air cavity, 400 μm thick sticky polymer spacers were placed in between a 1 mm thick glass slide and the substrate with the nanoposts. On the glass slide two 1 mm diameter holes were drilled using milling machine with diamond drill bit of 1 mm diameter to form the inlet and outlet of the microfluidic channel. Next, a photo-patternable polymer solution was prepared by mixing isobornyl acrylate (IBA), crosslinker tetraethylene glycol dimethacrylate, and photoinitiator−2,2−dimethoxy−2−phenylacetophenone at a weight ratio of 31.66 : 1.66 : 1. The solution was flown into the air cavity by means of a pipette through one of the drilled holes. Next, to prevent the channel from polymerization, a photomask was positioned over the glass slide and subsequently the device was exposed for about 60s to a UV light of intensity 12 mW cm^{-2}. Finally unpolymerized polymer solution was removed by washing with ethanol for few minutes. The final microfluidic biochip formed is shown in Fig. 2 and the schematic is illustrated in Fig. 3(f).

B. Sensor Functionalization

In order to immobilize the anti-PCT protein on the surface of the gold nanopost array, layers of graphene oxide (GO) and ligands were deposited by flowing them over the Au nanopost array. Colloidal solution of concentration 0.1 mg/mL was made using DI water followed by sonication to form single-layer graphene oxide nanosheets. 20 μL of the GO solution was introduced inside the microfluidic channel via the inlet. The GO solution is flown over the nanopost and kept at room temperature for 2 hr for drying. The GO nanosheets thus gets conforms to the shape of the nanoposts underneath it and this was confirmed from the SEM image of the fabricated GO/Au nanopost array illustrated in Fig. 4(b). At GO nanosheets, since there are ample functional groups viz. carboxylic and carbonyl etc., the GO layer serves as covalent binding site for the anti-PCT proteins. The covalent linkage was formed using EDC–NHS coupling chemistry [25]. To immobilize the ligands, a solution of 1: 1 volume ratio containing 1 mg/mL anti-PCT and EDC–NHS (EDC: 0.2 M; NHS: 0.05 M) was made. The surface of GO–Au nanoposts was covered by introducing 200 μL of the solution containing anti-PCT, EDC and NHS. The set up was kept inside a humid chamber for 12 hr at $4°C$. During this time, EDC reacts covalently with carboxyl groups present at the GO nanosheets forming an intermediate O-acylisourea. In the meantime another intermediate amine reactive stable NHS ester is produced by NHS that facilitates the association between the primary amines of anti-PCT by forming C–N covalent bonds. In order to prevent non-specific bindings and block the sites devoid of anti-PCT over the sensor surface, 2 mg/mL of bovine serum albumin (BSA) solution was introduced inside the channel. Finally the sensor surface is washed with the phosphate-buffered saline solution (PBS) of pH = 7.4. [29].

C. SPR Characterization and Simulation

Fig. 5(a) illustrates the simulation and experimental data comparison. After fabricating the nanopost array on the substrate, it was embedded in a microfluidic channel and the resonance was measured at 607 nm as shown by the green waveform. After coating a layer of graphene oxide on nanopost the resonant wavelength got shifted slightly by 1 nm (yellow waveform). Finally, after functionalizing the sensor with anti-PCT the resonance wavelength red shifted to 637 nm (shown by blue waveform).

COMSOL simulation, on the other hand, depicts that the resonance dip occurs at a wavelength of 614 nm prior to GO/anti-PCT functionalization, and at 635 nm after functionalization. The COMSOL-based FEM simulation was performed using the COMSOL Multiphysics 5.5. software as shown in Fig.5(c) and (d). In this simulation, periodic boundary conditions were applied at the boundaries in parallel to the light propagation direction. The top and bottom of the computation regions were placed with two perfectly matched layers (PMLs) so that all the scattered electromagnetic waves from the nanopost arrays were absorbed at the PMLs. In addition, the refractive index of the PMLs was set at the same value as of the surrounding media to simulate an infinitely thick substrate. Note since our analyte solution contains PCT which is a protein, the refractive index of the analyte solution was selected as 1.33 for simulation purpose.

The bulk index sensitivity of the fabricated gold nanoposts array was measured to be 470 nm per RIU by flowing water, acetone, ethanol, isopropyl alcohol, and chloroform with refractive indices 1.33, 1.36, 1.365, 1.377, and 1.44 respectively over the sensor surface illustrated in Fig. 5(b).

The main characteristics of the sensor is its resonance wavelength and the associated quality factor. An imperfection in sensor would affect both parameters, but it is only the quality factor that affects the sensor performance. As long as the resonance wavelength falls within the visible spectrum, its exact value is immaterial to sensor performance. In this sense, the sensor performance is unaffected by the pitch or depth of the nanoposts as long as the resonant wavelength remains within the realm of visible spectrum. The only things that can affect the quality factor (and hence the sensor performance) is the gold layer thickness, as discussed earlier in section-III which is optimized at thickness of 50 nm. A variation in that thickness will lead to lowering of sensor sensitivity. Further the thickness of functionalization Layers (GO, EDC-NHS, Anti-PCT) affect the reflectance minimum [30], that in turn affects the limit of detection of the sensor.

IV. EXPERIMENTAL SETUP AND SAMPLE PREPARATION

The experimental set up, illustrated in Fig. 6, consists of the fabricated microfluidic sensor chip (inset of Fig. 6), the optical source and detector module, a syringe pump to flow the sepsis biomarker (PCT), collecting vial at the output and a PC for real time data acquisition and analysis.

A. Instruments

For optical measurements, a white light source of power 150 watt quartz halogen lamp (Luxtec Fiber Optics, Plainsboro, NJ) was connected to a bifurcated optical fiber (BIF 400-VIS-NIR, Ocean Optics). A collimator (F220SMA-A from Thorlabs) was used to illuminate the nanoposts area inside the channel at normal incidence. The reflected light from the sensor surface was collected and measured by a UV/VIS spectrometer (USB-4000, Ocean Optics) attached to the other end of the bifurcated fiber. A syringe pump was used to inject the PCT solutions through the inlet of the microfluidic channel.

B. Chemicals and Sample Preparation

Materials used in sensor are ZUPA (Gelest, Inc.) nanoposts (pitch of 500 nm, height of 210 nm, and width of 250 nm), gold layer (50 nm thick), GO layer (20 nm thick), and anti-PCT layer (2 nm thick). Their refractive indices are: 1.470, 0.17689+ i3.47 (at 637nm), 1.9, 1.33 respectively. Lyophilized form of Procalcitonin (PCT), prepared at a 10 mM

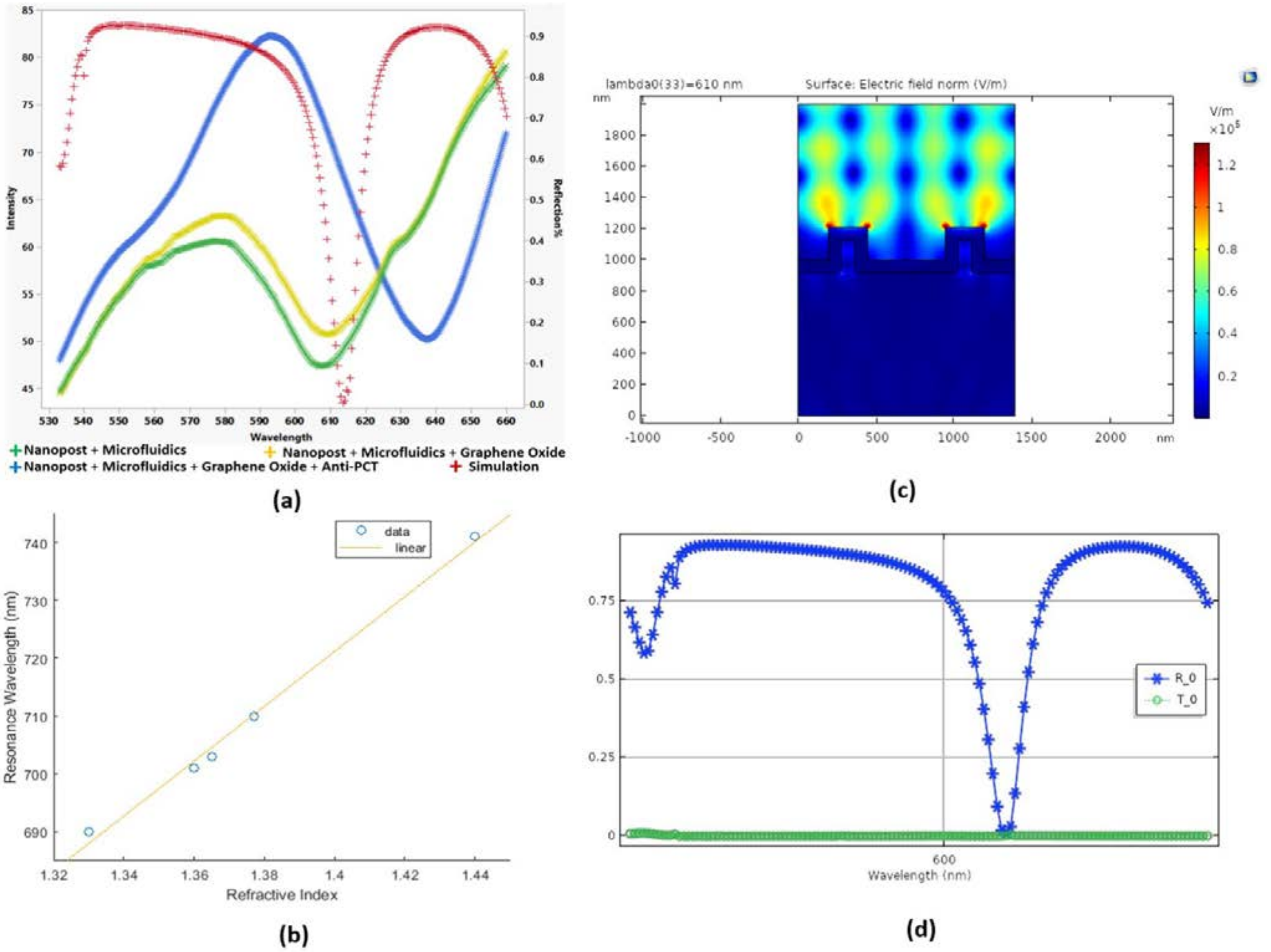

Fig. 5. Sensor Characterization (a) the resonance wavelength for the nanopost array embedded in a microfluidic channel is obtained at 607 nm. Red shift of 1 nm in SPR responses is depicted when Au nanoposts are coated with graphene oxide. After immobilization of anti-PCT over GO-Au nanoposts, the resonance red shifts to 637 nm. COMSOL simulation, depicts that the resonance dip is obtained at a wavelength of 614 nm prior to GO/anti-PCT functionalization and at 635 nm after functionalization. (b) Bulk RI sensitivity of the sensor w.r.t. different refractive index solutions (c) FEM simulation of the nanopost array using COMSOL Multiphysics 5.5. applying periodic boundary conditions at the boundaries in parallel to the light propagation direction. (d) Reflection spectrum of the simulated structure.

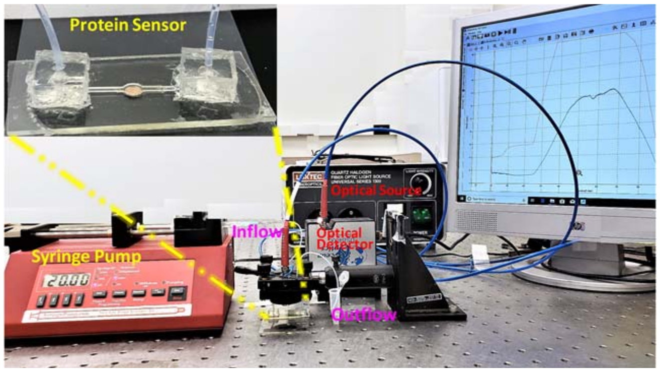

Fig. 6. Experimental setup.

sodium phosphate buffer and pH of 7.5, was procured from Millipore Sigma. The vial containing the PCT was centrifuged prior to use. Then it was reconstituted in sterile H_2O to a concentration of 0.1 mg/ml. This formed the stock solution which was further diluted to form different concentrations of PCT ranging from 10^5 pg/ml to 10 pg/ml. Deionized (DI) water (resistivity $>$ 18.2 MΩ-cm), used in our experiments was produced using a purification system from Millipore, Billerica, MA, USA. N-Ethyl N-(3-dimethylaminopropyl carbodiimide) (EDC) and N-hydroxysuccinimide (NHS) were obtained from Sigma Aldrich, MO, USA.

V. RESULTS AND DISCUSSIONS

A. Effect of Flow Rate on Analyte Capture

The specific capture of protein molecules depends not only on the sensor characteristics, but also on the flow rate. Increasing the flow rate reduces the protein capture time and imparts different amount of shear stress on the molecules, whereas decreasing the flow rate has reverse effect. Fig. 7(a) shows the effect of the flow rate (controlled by a syringe pump) on the specific absorption. When the flow rate was low, for instance 10 μL/min, the sensor surface required longer time (~30 min) to saturate, resulting in a low protein capture rate, as was measured in terms of rate of change of intensity

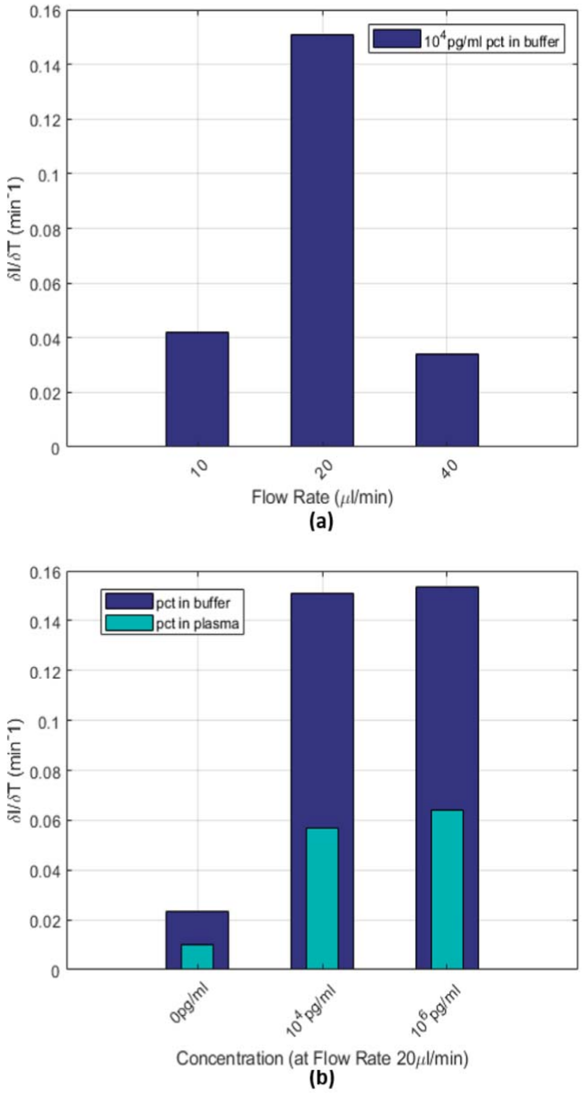

Fig. 7. Effect of flow rate on analyte capture and non-specifics (a) the flow rate of 20 μl min^{-1} provides maximum rate of change of sensor response to the protein PCT. (b) At the flow rate of 20 μl min^{-1} sensor response to protein PCT in buffer versus in plasma. The observed reduction in response in plasma gets addressed through calibration.

to be 0.04 min^{-1} (Fig. 7(a)). However, when the flow rate was raised to 20 μL/min, the sensor saturation took place within ~10 min, giving rise to higher rate of change of sensor response of ~0.15 min^{-1}. An even higher flow rate, namely, 40 μL/min, imparted higher shear stress on the molecules resulting in poor sensor response, and an even lower capture rate of ~0.03 min^{-1}. Thus, a flow rate of 20 μL/min was found to be optimal and selected for the sensing purpose. Fig. 7(b) shows the sensor response to non-specific absorption at this selected flow rate of 20 μL/min, when using BSA as the blocking agent.

We have evaluated the matrix effect and provided the sensor's response for 0, 10^4, and 10^6 pg/ml PCT prepared in buffer and plasma, as shown in Fig. 7(b). All three in-plasma readings are lower compared to the in-buffer readings. At 0 pg/ml, the sensor response is reduced by a factor of 2.33 for in-plasma w.r.t. in-buffer. There are reductions by factors of 2.64 and 2.4 at in 10^4 pg/ml and 10^6 pg/ml concentrations respectively. Thus the reduction in sensor's response in plasma is itself a concave curve (as can be seen in Fig. 7(b)), and this also gets addressed during calibration.

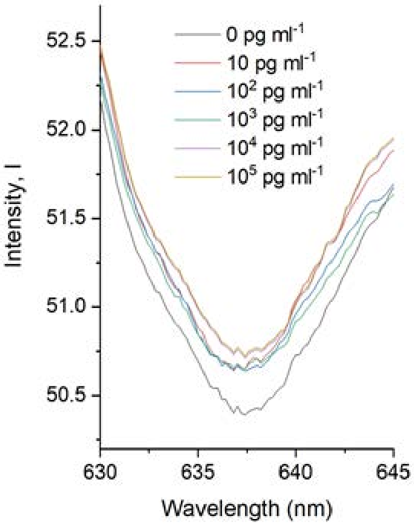

Fig. 8. SPR spectrum at six different PCT concentrations.

Lyophilized plasma sample prepared from pooled human blood was obtained from Sigma Aldrich (USA). No traces of PCT were found in the plasma as confirmed using the Synapt G2-Si H-Class UPLC Mass Spectrometer from Waters. The plasma was diluted with 1xPBS (pH = 7.4) buffer to prepare two different concentrations, 10^4 and 10^6 pg/ml. Both the plasma concentrations resulted in much lower sensor response as compared to the response due to PCT, thus further justifying the selection of 20 μL/min for our experiments.

B. Transient Response and Sensor Calibration Curve

As can be seen in Fig. 8, a reflection dip was found at the resonance wavelength of ~637 nm when the anti-PCT conjugated GO-Au nanoposts array was excited by the normal incident light. At this resonance wavelength of 637 nm the intensity measurements at various PCT concentrations were performed because the maximum intensity variation to the concentration change is realized at the resonance, justifying the design of an Au-coated nano-patterned sensor surface in the first place.

Fig. 8 depicts the reflection spectra of the SPR sensor for 5 different concentrations of PCT (10 pg/ml, 10^2 pg/ml, 10^3 pg/ml, 10^4 pg/ml, and 10^5 pg/ml) in the 1xPBS solution (pH = 7.4) in the visible region of the light spectrum from 630 nm to 645 nm. We specifically examine the five PCT concentrations around the resonant wavelength of 637 nm. As the PCT concentration increased from 0 pg/ml to 10 pg/ml, 10^2 pg/ml, 10^3 pg/ml, 10^4 pg/ml, and 10^5 pg/ml, the reflected light intensity increased by 0.23, 0.25, 0.26, 0.32 and 0.339, respectively. Each concentration of PCT solution was flown through the sensor surface for ~2 min at a flow rate of 20 μL/min, and intensity spectra were recorded.

TABLE I
COMPARISON OF OPTICAL TECHNIQUES TO DETECT SEPSIS BIOMARKERS (PCT,CRP,sTREM-1)

Principle	Sample	Biomarker	Interface	Sensitivity	Limit of Detection	References
Plasmonic (nanoparticles)	Buffer	CRP	Microarray (Nano Particle enhanced gold nanohole arrays)	0.1 a.u./pg.ml^{-1}	27 pg/ml	Altug et. al. [31]
Fiber Optic Evanescent Wave Excitation (FOEW)	Blood Plasma	PCT	Fiber optic nano-gold linked immunosorbent assay	0.024 a.u./pg.ml^{-1} *	0.095 pg/ml	Chiang et. al. [32]
Surface Plasmon Resonance (SPR)	Buffer, Simulated Blood Plasma	PCT	Molecular imprinted polymer surface	1.78 a.u./pg.ml^{-1}	9900 pg/ml	Denizli et al. [33]
Surface-Enhanced Raman Scattering (SERS)	Serum	PCT CRP sTREM 1	Au Coated MNPs	PCT (1.08 a.u./pM) * CRP (4.62 a.u./pM) * sTREM-1(1.69 a.u./pM) *	0.028 pg/ml (PCT) 0.0073 pg/ml(CRP) 0.00046 pg/ml(sTREM1)	Nguyen et al. [34]
Localized Surface Plasmon Resonance (LSPR)	Blood	PCT	Au Nanopillars	0.05 a.u./ pg.ml^{-1}	500 pg/ml	Deng et al. [35]
Surface Plasmon Resonance (SPR)	Buffer	PCT	Au Nanopost Array, Microfluidic	0.0643 a.u./ pg.ml^{-1} * at low conc. 0.0224 a.u./ pg.ml^{-1} * at higher conc.	1.22 pg/ml	This work

* Sensitivity is computed as change in intensity w.r.t. change in concentration in log scale

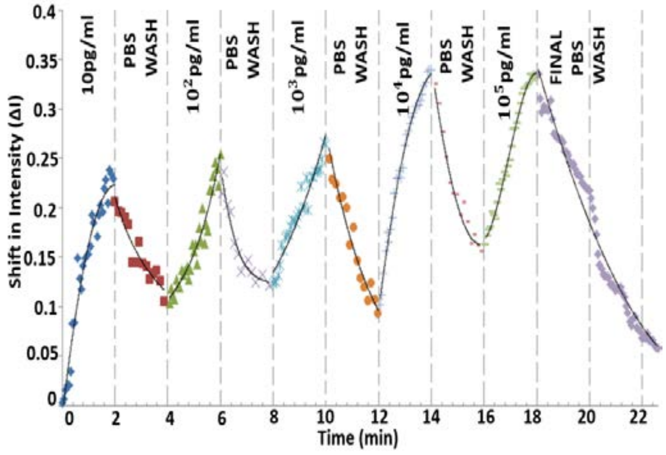

Fig. 9. Transient response for PCT molecules detection at the concentrations of 0 pg/ml, 10 pg/ml, 10^2 pg/ml, 10^3 pg/ml, 10^4 pg/ml and 10^5 pg/ml, depicting the association and dissociation phases for binding (antigen-antibody) interactions in the spiked 1xPBS solution of pH 7.4.

Fig. 9 demonstrates the ability of the sensor to optically track the binding kinetics as the PCT concentration increased from 0 pg/ml to 10 pg/ml, 10^2 pg/ml, 10^3 pg/ml, 10^4 pg/ml, and 10^5 pg/ml in the PBS solution. For this, the sensor surface was initially covered by the PBS solution, and then, the 10 pg/ml PCT solution was flown through the microfluidic channel for 2 min. This association phase induced an intensity rise by 0.23. Next, in the dissociation phase, sensor surface was washed with the PBS to remove the unbound or loosely bound PCT proteins from the nanopost surface, that resulted in intensity drop by 0.13. The association and dissociation phases were further repeated for the remaining concentrations of PCT. For each association phase, PCT solution was flown at a rate of 20 μL/min through the sensor surface for ~2 min, and without saturating the sensor surface. As the PCT concentration increased from 0 pg/ml to 10 pg/ml, 10^2 pg/ml, 10^3 pg/ml, 10^4 pg/ml, and 10^5 pg/ml, the reflection intensity increased by 0.24, 0.25, 0.26, 0.33 and 0.34, respectively, matching the results of Fig. 8 of the static setting. Finally, Fig. 10 shows the calibration curve that we generated from the measurement plot of Fig. 9, demonstrating how we used the measured data to perform the calibration between the logarithmic PCT concentrations and the SPR response for the 6 measured concentrations. The response is shifted toward the higher detected intensity with increase in concentration, that results from the specific binding of the PCT molecules over 2 min window each, and increase in the refractive index at the sensor surface.

Scientifically each data is represented as: "average value ± standard error", where the average and the standard error are of the same unit. Accordingly, Fig. 10 depicts the average value and the associated standard error at each concentration, where the standard errors at the concentrations 0 pg/ml to 10^5 pg/ml are computed to be 0.014, 0.008, 0.013, 0.008, 0.0178, and 0.0044, respectively. Using the average values, a calibration curve is fitted, where since the shift in intensity is higher at higher concentration, the fitted curve is chosen to be monotonicity increasing (the monotonicity also guarantees 1-1 mapping which is essential for calibration). The fitted curve is given by (7) having $R^2 = 0.97$:

$$I_\Delta = 0.2661\ [\log\ C]^{0.2417} - 0.05361, \tag{7}$$

where I_Δ denotes the intensity shift and C denotes the concentration. Equation (8) shows the sensitivity calculation from the fitted curve:

$$S_{I_\Delta,C} := \frac{d}{d\log C} I_\Delta = 0.0643\ [\log C]^{-.7583};$$
$$\Rightarrow S_{I_\Delta,C}|_{C=10\frac{pg}{ml}} = 0.0643;\ \ S_{I_\Delta,C}|_{C=10^4\frac{pg}{ml}} = 0.0224, \tag{8}$$

implying that at lower concentration of 10 pg/ml the sensitivity is 0.0643 a.u./ pg.ml^{-1}, and at higher concentration of 10^4 pg/ml it is 0.0224 a.u./ pg.ml^{-1} (concentrations are taken to be in log scale).

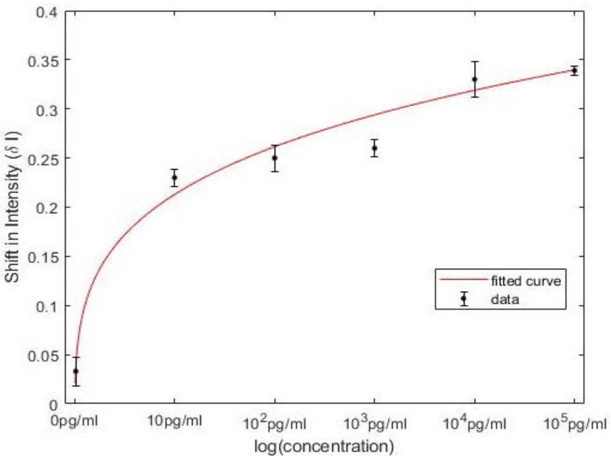

Fig. 10. Calibration Curve: SPR intensity shifts as a function of PCT concentrations in spiked PBS buffer; generated from the measurement plot in Fig. 9.

The Limit of Detection (LOD) is calculated from the fitted polynomial of the calibration curve as, $\frac{3\times \mathrm{SD}}{\mathrm{sensitivity}}\Big|_{10\frac{pg}{ml}} = \frac{3\times 0.02634}{0.0643} = 1.22$ pg.ml^{-1}. The coefficient of variation (CV%) values at concentrations 0 pg/ml to 10^5 pg/ml are 3.03%, 8.6%, 12%, 7.6%, 12.1%, 2.9% respectively. It should be noted that the sensor response relies on the interaction of the analyte (PCT) with a binding agent (anti-PCT), where the nature of protein-protein interaction leads to a nonlinear response, and these assays typically manifest greater variability [36]. Accordingly, per the regulating bodies like FDA (USA), EMA (Europe), MHLW (Japan), ANVISA (Brazil), for these protein binding assays, CV values $< 20\%$ are acceptable, making the CV values of our own sensor calibrator acceptable.

C. Performance Comparison

We compare the performance of our sensor with the other state of the art optical detection techniques for detecting sepsis biomarkers like PCT, CRP, sTREM-1, as enumerated in Table I. The sensitivity column has been reported based on the calibration curves provided by the authors in their respective works. While our sensor sensitivity is lower, it is still adequate for measurement and calibration as more importantly, it can measure over a much wider range, namely, 10 pg/ml to 10^5 pg/ml and that too in a POC setting. Also, the LOD of 1.22 pg.ml^{-1} is among the lowest reported: While [32] and [34] provide a slightly lower LOD, our sensor provides a portable and point-of-care solution, requiring little overhead of interfaced external devices or circuits for an integrated system. The achieved sensitivity, range, and LOD of our biosensor are thus remarkable for POC setting, and stand out in comparison to other reported techniques where biomarkers were also spiked in a buffered solution. Further since our biosensor is microfluidics based, our sensor can be easily integrated to render the measured protein in other samples, viz. blood, serum, etc. These validate that our sensor serves as a good proof-of-principle plasmonic microfluidic biochip for POC sepsis biomarker detection.

VI. CONCLUSION

To summarize the work, we have developed a novel microfluidic plasmonic device for real-time and label-free detection of a sepsis biomarker for POC application. The label-free detection of PCT reduces the detection time as compared to conventional labeled detection methodologies, and also portable biochip design makes it suitable for eventual POC application by integration with optics for excitation and measurement. Since our methodology involves detection of variations in intensity of the visible light reflected from the sensor surface, inexpensive source and detector can be integrated in a package to make the device portable and serve as a POC instrument for sepsis biomarker quantification. Future work will involve multiplexed detection of other sepsis biomarkers in a single chip, and design and fabrication of an integrated POC sensing system.

ACKNOWLEDGMENT

The authors would like to thank the Electronics Technology Group, Department of Electrical and Computer Engineering (ECE), Iowa State University (ISU), for assistance with various logistics related to seamless execution of experiments, and to the Materials Analysis and Research Laboratory at ISU for imaging facilities.

REFERENCES

[1] C. Fleischmann *et al.*, "Assessment of global incidence and mortality of hospital-treated sepsis. Current estimates and limitations," *Amer. J. Respiratory Crit. Care Med.*, vol. 193, no. 3, pp. 259–272, Feb. 2016.

[2] C. Fleischmann-Struzek, D. M. Goldfarb, P. Schlattmann, L. J. Schlapbach, K. Reinhart, and N. Kissoon, "The global burden of paediatric and neonatal sepsis: A systematic review," *Lancet Respiratory Med.*, vol. 6, no. 3, pp. 223–230, Mar. 2018.

[3] R. Daniels, "Surviving the first hours in sepsis: Getting the basics right (an intensivist's perspective)," *J. Antimicrobial Chemotherapy*, vol. 66, no. 2, pp. ii11–ii23, Apr. 2011.

[4] S. Kundu, S. Tabassum, and R. Kumar, "A perspective on sepsis pathogenesis, biomarkers and diagnosis: A concise survey," *Med. Devices Sensors*, vol. 3, no. 4, Aug. 2020, Art. no. e10089.

[5] S. E. Beekmann, D. J. Diekema, K. C. Chapin, and G. V. Doern, "Effects of rapid detection of bloodstream infections on length of hospitalization and hospital charges," *J. Clin. Microbiol.*, vol. 41, no. 7, pp. 3119–3125, Jul. 2003.

[6] A. Linnér, J. Sundén-Cullberg, L. Johansson, H. Hjelmqvist, A. Norrby-Teglund, and C. J. Treutiger, "Short- and long-term mortality in severe sepsis/septic shock in a setting with low antibiotic resistance: A prospective observational study in a Swedish university hospital," *Frontiers Public Health*, vol. 1, p. 51, Nov. 2013.

[7] E. Bouza, D. Sousa, M. Rodríguez-Créixems, J. G. Lechuz, and P. Munoz, "Is the volume of blood cultured still a significant factor in the diagnosis of bloodstream infections?" *J. Clin. Microbiol.*, vol. 45, no. 9, pp. 2765–2769, 2007.

[8] D. C. Angus and T. Van der Poll, "Severe sepsis and septic shock," *New England J. Med.*, vol. 369, pp. 840–851, Aug. 2013.

[9] C. Russell *et al.*, "Development of a needle shaped microelectrode for electrochemical detection of the sepsis biomarker interleukin-6 (IL-6) in real time," *Biosensors Bioelectron.*, vol. 126, pp. 806–814, Feb. 2019.

[10] P. Dey *et al.*, "Label-free bacteria quantification in blood plasma by a bioprinted microarray based interferometric point-of-care device," *ACS Sensors*, vol. 4, no. 1, pp. 52–60, Jan. 2019.

[11] E. Macchia *et al.*, "Selective single-molecule analytical detection of C-reactive protein in saliva with an organic transistor," *Anal. Bioanal. Chem.*, vol. 411, no. 19, pp. 4899–4908, Jul. 2019.

[12] P. Ohlsson, K. Petersson, P. Augustsson, and T. Laurell, "Acoustic impedance matched buffers enable separation of bacteria from blood cells at high cell concentrations," *Sci. Rep.*, vol. 8, no. 1, pp. 1–11, Dec. 2018.

[13] F. Ellett *et al.*, "Diagnosis of sepsis from a drop of blood by measurement of spontaneous neutrophil motility in a microfluidic assay," *Nature Biomed. Eng.*, vol. 2, no. 4, p. 207, 2018.

[14] H. Im, J. N. Sutherland, J. A. Maynard, and S.-H. Oh, "Nanohole-based surface plasmon resonance instruments with improved spectral resolution quantify a broad range of antibody-ligand binding kinetics," *Anal. Chem.*, vol. 84, no. 4, pp. 1941–1947, Feb. 2012.

[15] S.-F. Joe, L.-Z. Hsieh, L.-B. Chang, C.-M. Hsu, and C.-M. Wu, "Kinetic analysis of antibody–antigen interactions using phase-detection-based surface plasmon resonance sensor system," *Jpn. J. Appl. Phys.*, vol. 46, no. 5R, p. 3114, 2007.

[16] K. Reinhart, M. Bauer, N. C. Riedemann, and C. S. Hartog, "New approaches to sepsis: Molecular diagnostics and biomarkers," *Clin. Microbiol. Rev.*, vol. 25, no. 4, pp. 609–634, Oct. 2012.

[17] C. Dixon, J. Lamanna, and A. R. Wheeler, "Direct loading of blood for plasma separation and diagnostic assays on a digital microfluidic device," *Lab Chip*, vol. 20, no. 10, pp. 1845–1855, 2020.

[18] S. Yang, A. Ündar, and J. D. Zahn, "A microfluidic device for continuous, real time blood plasma separation," *Lab Chip*, vol. 6, no. 7, pp. 871–880, 2006.

[19] U. Neugebauer, S. Trenkmann, T. Bocklitz, D. Schmerler, M. Kiehntopf, and J. Popp, "Fast differentiation of SIRS and sepsis from blood plasma of ICU patients using Raman spectroscopy," *J. Biophotonics*, vol. 7, nos. 3–4, pp. 232–240, Apr. 2014.

[20] S. Shenoy, "Exosomal microRNA as a sepsis biomarker: Assessing different volumes of plasma for possible quantification of exosomal microRNA," Med. Health Sci., Biosci.-Mol. Biodesign, Tech. Rep., 2019, p. 28. [Online]. Available: https://www.diva-portal.org/smash/record.jsf?pid=diva2%3A1342044&dswid=756

[21] N. Fabri-Faja *et al.*, "Early sepsis diagnosis via protein and miRNA biomarkers using a novel point-of-care photonic biosensor," *Analytica Chim. Acta*, vol. 1077, pp. 232–242, Oct. 2019.

[22] H. Ghaemi, T. Thio, D. E. A. Grupp, T. W. Ebbesen, and H. Lezec, "Surface plasmons enhance optical transmission through subwavelength holes," *Phys. Rev. B, Condens. Matter*, vol. 58, no. 11, p. 6779, 1998.

[23] H. Raether, *Surface Plasmons* (Springer-Verlag Tracts in Modern Physics), vol. 111. New York, NY, USA: Springer-Verlag, 1988. [Online]. Available: http://www.fulviofrisone.com/attachments/article/406/raether_2.pdf

[24] D. Sarid and W. A. Challener, *Modern Introduction to Surface Plasmons: Theory, Mathematica Modeling, and Applications*. Cambridge, U.K.: Cambridge Univ. Press, 2010.

[25] M. A. Ali *et al.*, "*In situ* integration of graphene foam–titanium nitride based bio-scaffolds and microfluidic structures for soil nutrient sensors," *Lab Chip*, vol. 17, no. 2, pp. 274–285, 2017.

[26] S. M. A. Uddin, S. S. Chowdhury, and E. Kabir, "A theoretical model for determination of optimum metal thickness in kretschmann configuration based surface plasmon resonance biosensors," in *Proc. Int. Conf. Electr., Comput. Commun. Eng. (ECCE)*, Feb. 2017, pp. 651–654.

[27] L. Dong, A. K. Agarwal, D. J. Beebe, and H. Jiang, "Adaptive liquid microlenses activated by stimuli-responsive hydrogels," *Nature*, vol. 442, no. 7102, pp. 551–554, Aug. 2006.

[28] D. J. Beebe *et al.*, "Microfluidic tectonics: A comprehensive construction platform for microfluidic systems," *Proc. Nat. Acad. Sci. USA*, vol. 97, no. 25, pp. 13488–13493, Dec. 2000.

[29] M. A. Ali, S. Tabassum, Q. Wang, Y. Wang, R. Kumar, and L. Dong, "Integrated dual-modality microfluidic sensor for biomarker detection using lithographic plasmonic crystal," *Lab Chip*, vol. 18, no. 5, pp. 803–817, 2018.

[30] F. Usman *et al.*, "Enhanced sensitivity of surface plasmon resonance biosensor functionalized with doped polyaniline composites for the detection of low-concentration acetone vapour," *J. Sensors*, vol. 2019, pp. 1–13, Nov. 2019.

[31] A. Belushkin, F. Yesilkoy, and H. Altug, "Nanoparticle-enhanced plasmonic biosensor for digital biomarker detection in a microarray," *ACS Nano*, vol. 12, no. 5, pp. 4453–4461, May 2018.

[32] C.-Y. Chiang *et al.*, "Fiber optic nanogold-linked immunosorbent assay for rapid detection of procalcitonin at femtomolar concentration level," *Biosensors Bioelectron.*, vol. 151, Mar. 2020, Art. no. 111871.

[33] G. Sener, E. Ozgur, A. Y. Rad, L. Uzun, R. Say, and A. Denizli, "Rapid real-time detection of procalcitonin using a microcontact imprinted surface plasmon resonance biosensor," *Analyst*, vol. 138, no. 21, pp. 6422–6428, Nov. 2013.

[34] A. H. Nguyen, Y. Shin, and S. J. Sim, "Development of SERS substrate using phage-based magnetic template for triplex assay in sepsis diagnosis," *Biosensors Bioelectron.*, vol. 85, pp. 522–528, Nov. 2016.

[35] L. L. Sun, Y. S. Leo, X. Zhou, W. Ng, T. I. Wong, and J. Deng, "Localized surface plasmon resonance based point-of-care system for sepsis diagnosis," *Mater. Sci. Energy Technol.*, vol. 3, pp. 274–281, Jan. 2020.

[36] M. Azadeh *et al.*, "Calibration curves in quantitative ligand binding assays: Recommendations and best practices for preparation, design, and editing of calibration curves," *AAPS J.*, vol. 20, no. 1, pp. 1–16, Jan. 2018.

Souvik Kundu received the B.Tech. degree in electronics and communication engineering from the West Bengal University of Technology, Kolkata, India, in 2011, the M.Tech. degree in VLSI and microelectronics from Jadavpur University, Kolkata, in 2014, and the M.S. degree in microelectronics and photonics from Iowa State University, Ames, USA, in 2019, where he is currently pursuing the Ph.D. degree in bioengineering with the Electrical and Computer Engineering Department. His current research interests include biosensensing, modeling, fabrication, characterization of sensors, and clinical data analysis. He was a recipient of the Institute Fellowship from the Indian Institute of Engineering Science and Technology, Howrah, India, from 2015 to 2017. He was also a recipient of the Teaching Excellence Award from the Graduate College (for two times), Iowa State University, in 2018 and 2020, for his outstanding contribution to teaching.

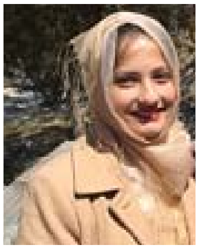

Shawana Tabassum received the B.Sc. degree in electrical engineering from the Bangladesh University of Engineering and Technology, Bangladesh, in 2014, and the Ph.D. degree in electrical and computer engineering from the Iowa State University (ISU), Ames, IA, USA, in 2018. She is an Assistant Professor of Electrical Engineering at The University of Texas at Tyler, where she directs the Laboratory for Integrated Micro-nano Biodevices. was a recipient of the Science Breakthrough of the Year: the Emerging Talent from Falling Walls in 2020, the Robert J. Menges Award for outstanding research in educational development in 2020, the Postdoctoral Scholar Excellence Award for teaching and mentoring students in 2020, the Best Global Impact Innovation Prize from ISU's Pappajohn Center for Entrepreneurship in 2019, the Biomedical Engineering Society's Career Development Award in 2019, the Research Excellence Award in 2018, and a Finalist of the Best Paper Award at IEEE Sensors Conference (2016).

Ratnesh Kumar (Fellow, IEEE) received the B.Tech. degree in electrical engineering from IIT Kanpur, India, in 1987, and the M.S. and Ph.D. degrees in electrical and computer engineering from The University of Texas at Austin, in 1989 and 1991, respectively. He is a Harpole Professor of Electrical and Computer Engineering at Iowa State University, where he directs the Embedded Software, Sensors, Networks, Cyberphysical, and Energy (ESSeNCE) Laboratory. Previously, he held a faulty position at the University of Kentucky and various visiting positions with the University of Maryland, College Park; the Applied Research Laboratory, Pennsylvania State University, State College; NASA Ames; the Idaho National Laboratory; United Technologies Research Center; and Air Force Research Laboratory. He is a Fellow of AAAS. He was a recipient of the D. R. Boylan Eminent Faculty Award for Research from Iowa State University, the Gold Medals for the Best EE Undergraduate, the Best EE Project, the Best All Rounder from IIT Kanpur, the Best Dissertation Award from UT Austin, the Best Paper Award from the IEEE Transactions on Automation Science and Engineering, and a keynote speaker and the paper awards recipient from multiple conferences. He was a Distinguished Lecturer of the IEEE Control Systems Society. He has been an Editor of several journals, including IEEE, SIAM, ACM, Springer, IET, and MDPI.